LAWRENCE
LIVERMORE
NATIONAL
LABORATORY

UCRL-CONF-213499

Simulation of penetration into porous geologic media

O. Y. Vorobiev, B. T. Liu, I. N. Lomov, T. Antoun

July 11, 2005

HVIS
Squaw Creek, CA, United States
October 10, 2005 through October 14, 2005

Disclaimer

Simulation of penetration into porous geologic media

Vorobiev O.Yu, Liu B.T, Lomov I.N and Antoun T.H

Lawrence Livermore National Laboratory

L-206, P.O. Box 808, Livermore, CA 94550, USA

Abstract

We present a computational study on the penetration of steel projectiles into porous geologic materials. The purpose of the study is to extend the range of applicability of a recently developed constitutive model to simulations involving projectile penetration into geologic media. The constitutive model is non-linear, thermodynamically consistent, and properly invariant under superposed rigid body motions. The equations are valid for large deformations and they are hyperelastic in the sense that the stress tensor is related to a derivative of the Helmholtz free energy. The model uses the mathematical structure of plasticity theory to capture the basic features of the mechanical response of geological materials including the effects of bulking, yielding, damage, porous compaction and loading rate on the material response. The new constitutive model has been successfully used to simulate static laboratory tests under a wide range of triaxial loading conditions, and dynamic spherical wave propagation tests in both dry and saturated geologic media.

Keywords: penetration, constitutive modeling, numerical simulations, porous compaction, dilatancy, poroelasticity, spherical cavity expansion.

1. Introduction

In this paper we demonstrate that the same model that has successfully been used to represent static data, as well as small scale and large scale wave propagation data can be used to simulate penetration into geologic media. A series of simulations are performed under a range of impact conditions, and the results are compared to experimental data up to impact velocities of about 1 km/s.

2. Model for porous geologic media

2.1 Basic equations

The thermomechanical structure of the model for partially saturated geological is based on the developments in [1]. Within this context, an elemental volume dv of the porous material in the present configuration is expresses as the sum of solid volume dv_s and pore volume dv_p, such that

$$dv = dv_s + dv_p \ , \ dV = dV_s + dV_p \ , \quad (1)$$

where $\{dV, dV_s, dV_p\}$ are the values of $\{dv, dv_s, dv_p\}$, respectively, in a fixed reference configuration. The porosity ϕ and its reference value Φ are defined by

$$\phi = \frac{dv_p}{dv} \ , \ \Phi = \frac{dV_p}{dV} \ . \quad (2)$$

The total dilatation, J, and the average dilatation of the solid, J_s, are defined by

$$J = \frac{dv}{dV} \ , \ J_s = \frac{dv_s}{dV_s} = \left[\frac{1-\phi}{1-\Phi}\right] J \ , \qquad (3)$$

The elastic response of the solid is characterized by the dilatation, J_s, in (3) where the total dilatation, J, is determined by the evolution equation

$$\frac{\dot{J}}{J} = \mathbf{D} \bullet \mathbf{I}, \qquad (4)$$

where **D** is the symmetric part of the velocity gradient **L**, and the superposed dot denotes material time differentiation. A symmetric unimodular tensor $\mathbf{B}'_e$ is used as a measure of pure elastic distortion in the evolution equation

$$\dot{\mathbf{B}}'_e = \mathbf{L}\mathbf{B}'_e + \mathbf{B}'_e\mathbf{L}^T - \frac{2}{3}(\mathbf{D} \bullet \mathbf{I})\,\mathbf{B}'_e - \mathbf{A}_p\,, \quad \mathbf{A}_p = \Gamma_p\left[\mathbf{B}'_e - \left\{\frac{3}{\mathbf{B}'^{-1}_e \bullet \mathbf{I}}\right\}\mathbf{I}\right], \qquad (5)$$

where the tensor, $\mathbf{A}_p$, characterizes the direction and magnitude of inelasticity for distortional response and Γ_p requires an additional constitutive equation, (see [1] for example.)

We introduce poroelasticity by expressing the porosity as a function of J and a history dependent variable ϕ_u (similar to [1]) as

$$\phi = \phi_u\left[1 - \frac{ax}{b(1+x)}\right],\ x = \frac{b(1-\phi_u)(J_u/J - 1)}{\phi_u},\ J_u = \frac{1-\Phi}{1-\phi_u},\ 0 \le a < 1,\ 0 \le a/b < 1 \qquad (6)$$

where ϕ_u is the unloaded porosity, x is auxiliary variable and {a,b} are material constants. The unloaded porosity ϕ_u describes the porosity that would exist if the material was unloaded from the current state.

2.2 Yield Surface

Geologic media are frictional materials and as such, their yield behavior is pressure dependent. The current model introduces two pressure dependent surfaces that govern the

material response during yielding: the initial yield surface (onset of yield), $Y_0(p)$, and the ultimate strength surface, $Y_f(p)$, (see Figure 1). The yield strength corresponding to a generalized triaxial compression state, $Y_{TXC}(p)$, is derived from $Y_0(p)$ and $Y_f(p)$ such that

$$Y_{TXC} = \delta_h\, Y_f(p) + (1-\delta_h)\, Y_0(p). \qquad (7)$$

The equivalent plastic strain ε_p, determined by integrating the evolution equation

$$\dot{\varepsilon}_p = \left[\frac{2}{3}\,\mathbf{D}_p \bullet \mathbf{D}_p\right]^{1/2}, \quad \mathbf{D}_p = \frac{1}{2}\,\Gamma_p\,\mathbf{A}_p \approx \frac{1}{2}\,\Gamma_p\,\mathbf{B}''_e\,, \qquad (8)$$

is used to define a hardening parameter δ_h

$$\delta_h = \frac{\varepsilon_p}{\varepsilon_{hard} + \varepsilon_p}\,, \qquad (9)$$

where ε_{hard} is a constant. The initial yield surface is expressed in the form

$$Y_0(p) = C\, Y_f(p) \left[\frac{P_c - \max(P_0,p)}{P_c - P_0}\right]^r, \; 0 < C \le 1,\; r > 1, \qquad (10)$$

where $\{C, r\}$ are constants and $\{P_0, P_c\}$ are functions of compaction to be specified.

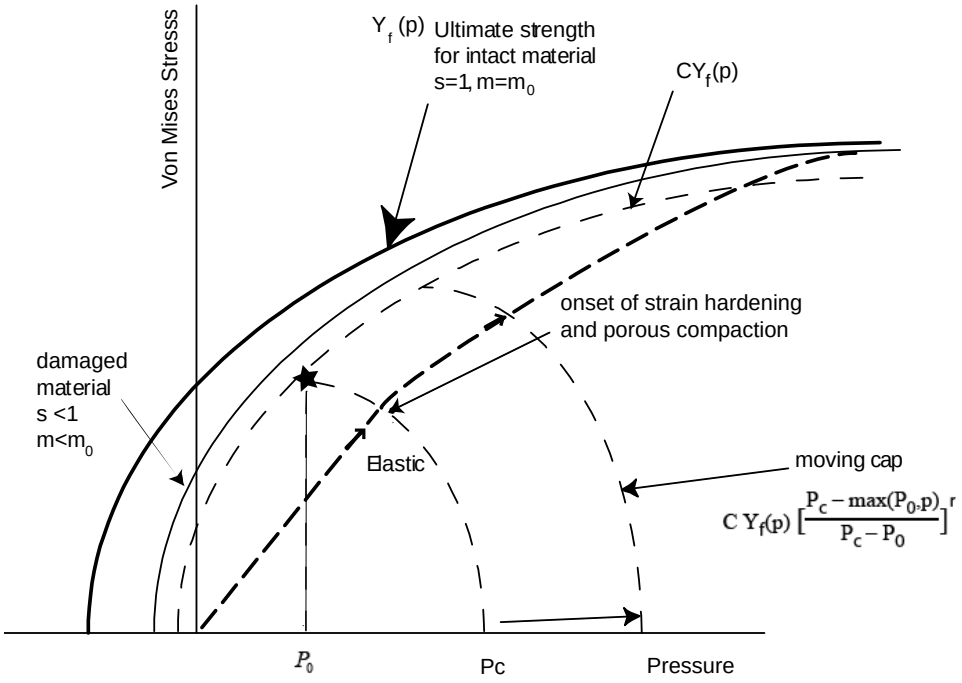

Fig. 1 Yield surface in Y-P plane. The cap separating elastic and plastic regions on the right moves with compaction. The pressure corresponding to the beginning of compaction in hydrostatic conditions Pc is defined by the compaction curve. Uniaxial strain loading path is shown with the bold dashed line.

The ultimate strength function is based on the Hoek and Brown (H&B) [2,3] strength criterion that relates the maximum (σ_1) and minimum (σ_3) principal stress on the failure surface as

$$\sigma_1 = \sigma_3 + Y_c\left(m\frac{\sigma_3}{Y_c} + s \right)^n \qquad (11)$$

For most rocks ½ is a reasonable value for *n*. Parameter *s* is equal to unity for intact material and less than unity for *in situ* material. Hoek [4] gives an empirical relationship between the coefficients, *s* and *m* and the Geologic Strength Index (GSI)

$$s = \exp\left(\frac{GSI - 100}{9} \right) \qquad (12)$$

$$m = m_i \exp\left(\frac{GSI - 100}{28}\right) \qquad (13)$$

In (13), m_i is the value of m for intact rock; it can be obtained from static lab tests.

For triaxial compression with $\sigma_e = Y_f$, the principal stresses σ_1 and σ_3 are given by

$$\sigma_1 - \sigma_3 = Y_f, \ \sigma_3 = p - \frac{Y_f}{3}, \qquad (14)$$

so that the H&B function (12) yields

$$\frac{Y_f}{Y_c} = \left[s + \frac{m\,p}{Y_c} - \frac{m\,Y_f}{3Y_c}\right]^n, \qquad (15)$$

When n=0.5, Eq. (15) becomes a quadratic equation and the failure strength Y_f can be expressed in terms of pressure and unconfined compressive strength Y_c as

$$Y_f = Y_c\left[\sqrt{s + \frac{m^2}{36} + \frac{mP}{Y_c}} - \frac{m}{6}\right] \qquad (16)$$

For the more general case where $n \neq 0.5$, Eq. (16) takes the form:

$$Y_f = Y_c\left[\left(s + \frac{m^2}{36} + \frac{mP}{Y_c}\right)^n + s^n - \left(s + \frac{m^2}{36} + \frac{m}{3}s^n\right)^n\right] \qquad (17)$$

We use a measure of damage, Ω expressed through ϕ_2, the total amount of bulking porosity (dilatancy) generated in the material, as

$$\Omega = \frac{\langle \phi_2 - \phi_{cr} \rangle D}{1 + \langle \phi_2 - \phi_{cr} \rangle D}, 0 < \Omega < 1, \qquad (18)$$

where D is the rate of softening. As damage accumulates during loading, the material softens. This is expressed mathematically in the model by making m and s functions of

damage. For simplicity, we use the same functional form as the empirical law relating those parameters to the Geologic Strength Index:

$$s = s_0 \exp\left(\frac{-100\Omega}{9}\right);\ m\ = m_0 \exp\left(\frac{-100\Omega}{28}\right) \qquad (19)$$

The function P_0 that defines the point of intersection of the onset of yield surface (Y_0 in (10)) and the hardening cap (see Figure 1) is specified in terms of the compaction pressure P_c by the form

$$P_0 = \alpha\, P_{c0} + \beta\, (P_c - P_{c0})\,, \qquad (20)$$

where $\{0<\alpha<1,\ 0<\beta<1\}$ are constants and P_{c0} is the value of P_c in the reference configuration defined as $P_{c0} = K\mu_c$. (21)

The value of α can be determined by iteratively solving the equation

$$\frac{4}{3}\,\alpha P_{c0} = C\, Y_f(\alpha P_{c0}), \quad (22)$$

which specifies the intersection of the lower end of Mogi line [5] with the onset curve $Y_0(p)$.

Strain rate scaling is introduced by defining a function $R(\dot{\varepsilon})$ of the equivalent total strain rate

$$\dot{\varepsilon} = \sqrt{\frac{2}{3}\,\mathbf{D}' \bullet \mathbf{D}'}\ , \quad \mathbf{D}' = \mathbf{D} - \frac{1}{3}\,(\mathbf{D} \bullet \mathbf{I})\,\mathbf{I} \qquad (23)$$

The following function of form was used for R

$$R = \left(1 + \frac{\dot{\varepsilon}}{\dot{\varepsilon}_0}\right)^m \quad (24)$$

The final yield surface including loading direction effects and the rate effects similarly to [6] and takes the form

$$Y = R(\dot{\varepsilon})Y_{TXC}(p / R(\dot{\varepsilon}))F(\beta), \qquad (25)$$

where $F(\beta)$ is a function of the Lode angle described in [8].

2.3 Porous compaction and dilation

Porosity changes in the model are described in terms of three source terms as

$$\dot{\phi}_u = \dot{\phi}_1 + \dot{\phi}_2 + \dot{\phi}_3, \qquad (26)$$

$\dot{\phi}_1$ describes compaction of the intact material, $\dot{\phi}_2$ describes dilatancy, or bulking, and $\dot{\phi}_3$ describes changes in *in situ* porosity associated with fractures and other inhomogeneities in the medium[2].

Compaction of the primary porosity is described using target porosity ϕ_1^*, which defines the compaction curve under quasi-static loading:

$$\dot{\phi}_1 = \left\langle \phi_1 - \phi_1^* \right\rangle / \tau_p, \qquad (27)$$

where τ_p is a function of the deformation rate representing a characteristic time for compaction, , and $\phi_1^*(\hat{\mu})$ is a function of adjusted compression.

For simplicity, we assume that the reference compaction curve is a linear function of adjusted compression as

---

[2] The present study considers only intact material behavior. The model for secondary porosity will not be discussed further in this paper.

$$\phi_1^*(\hat{\mu}) = \Phi - S(1-\Phi)\langle \hat{\mu} - \mu_c \rangle, \hat{\mu} = \mu - \mu_e + \mu_s - \mu_b \qquad (28)$$

The compression shifts μ_e, μ_s, μ_b describe effects of heating (μ_e), shear enhanced compaction (μ_s) and bulking (μ_b). The value of μ_ε can be found by inverting the EOS as

$$\mu_e = \varepsilon / \left((1-\Phi)(\partial p_s / \partial \rho)_\zeta \right) \qquad (29)$$

Functions μ_s and μ_b are described below.

2.3.1 Bulking shift.

The volumetric strain shift associated with bulking, μ_b, is an increasing function of bulking porosity specified by the user. This parameter is a measure of the amount of bulking porosity that can be recompacted in subsequent loading. If μ_b=0, then all the bulking porosity can be recompacted in compression. To ensure continuity in the compaction response, the maximum shift of the compaction curve associated with bulking should not exceed the value

$$\mu_{\max} = -\phi_2 / \left(\frac{\partial \phi}{\partial \mu} \right) \qquad (30)$$

For the linear compaction behavior expressed in Eq. (28) the bulking shift can be expressed as a fraction of the maximum shift

$$\mu_b = \overline{\gamma} \mu_{\max} = \frac{\overline{\gamma} \phi_2}{S(1-\Phi)} = \gamma \phi_2, \qquad (31)$$
$$\gamma = \overline{\gamma} / (S(1-\Phi)).$$

Parameter γ in Eq. (31) defines the fraction of the bulking porosity that is compacted together with incipient porosity.

2.3.2 Bulking rate

The bulking (dilatancy) rate is specified as:

$$\dot{\phi}_2 = A\frac{dY}{dp}\dot{\varepsilon}_p(1-\phi), \qquad A = \frac{A_0 + \frac{dY}{dp}A_1}{1+\frac{dY}{dp}} \tag{32}$$

where the functional form for A is chosen to allow for variable dilatancy with A_0 specifying the degree of associativity at high pressures, where the dependence of the yield strength on pressure is generally not very strong, and A_1 specifying the degree of associativity at low pressures, where the yield strength is generally a strong function of pressure. In both cases, A=1 corresponds to fully associative flow.

2.3.4 Shear-enhanced compaction.

To make compaction consistent with the yield surface we need to find a function $\hat{\mu}_s$ that would make the onset of compaction and yielding simultaneous. The shift can be expressed in terms of cap size assuming constant bulk modulus as

$$\mu_s = \frac{P_c - P_0}{K}\left(\frac{\sigma_e}{CY_f(p)}\right)^{1/l}, \tag{33}$$

where the compaction pressure P_c is expressed using a linear compaction curve as

$$P_c = p + K\left(\frac{\Phi-\phi}{S(1-\phi)} + \mu_c + \mu_e + \mu_b - \mu\right). \tag{34}$$

According to (28) and , (33), compaction will start earlier in the presence of deviatoric stresses, at about the same time as yielding. The rate of compaction is defined primarily by the slope *S*. To reduce the number of model parameters we used the assumption that at full compaction the material has the same density regardless of the loading path, which gives the following expression for the slope *S*

$$S = \frac{\Phi S_0}{\Phi + \mu_s S_0 (1-\Phi)}. \qquad (35)$$

Since both P_c and Y_f vary during compaction, we use corrections proportional to the projected porosity change to account for these changes. Thus in (36) we use corrected values of P_c and Y_f taken as

$$\begin{aligned} P_c' &= P_c + K(\phi - \phi^*)\frac{(1-S+S\Phi)}{S(1-\Phi)} \\ Y_f'(p) &= Y_f(p) - \frac{dY}{dp}(\phi - \phi^*)K \end{aligned}, \qquad (36)$$

where ϕ^* is a trial target porosity calculated without corrections from the compaction curve (28). Figure 2 below illustrates the dependence of the compaction slope on μ_s

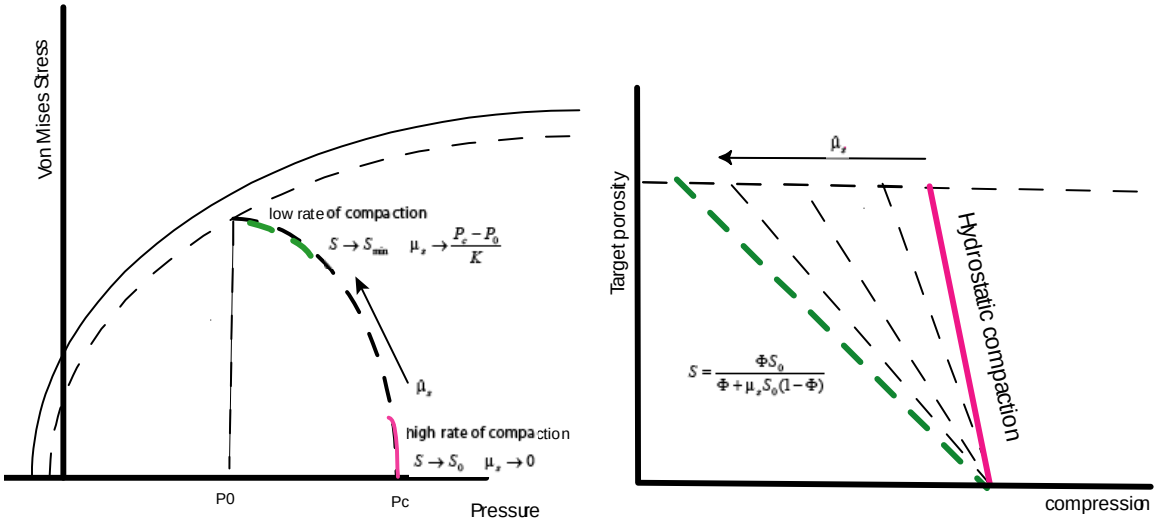

Fig.2. Dependence of the target curve on the shear enhanced compaction μ_s.

2.4 Numerical integration and hardening corrections

Since the strength of geologic materials exhibits a strong sensitivity to plastic strain and pressure, stable integration of the constitutive equations for these materials is very important. Due to strong nonlinearity of material behavior implicit integration may be

required in the general case. However, in most cases it is possible to avoid costly iterations by applying an explicit integration algorithm that accounts for the first order effects of plastic-strain and pressure hardening (e.g., see [7]).

To update the state of material at a given arbitrary time step, we use the following sequence of steps:

1. **Porous compaction**

   Calculate a new value of P_c as described above. Adjust the pressure due to porosity change.

2. **Yield strength calculation**

   Calculate new strength using cap factor found in the previous step as well as new derivatives $\frac{\partial Y}{\partial P}$ and $\frac{\partial Y}{\partial \varepsilon_p}$, which are used in the following steps.

3. **New shear modulus calculation**

   Calculate new shear modulus using new bulk modulus and Poisson ratio.

4. **Bulking rate calculation**

   Calculate bulking rate using new $\frac{\partial Y}{\partial P}$ and pressure corrected for porous compaction.

5. **Stress update and plastic strain calculation**

   The integration scheme described in [8] uses the radial return method and determines the final value of elastic distortional deformation $\mathbf{B}'_{\mathbf{e}}$ in terms of an elastic trial values $\mathbf{B}''^{*}_{\mathbf{e}}$ and $\sigma^{*}_{\mathbf{e}}$ of $\mathbf{B}''_{\mathbf{e}}$ and $\sigma_{\mathbf{e}}$ respectively as

   $$\mathbf{B}''^{*}_{\mathbf{e}} = \lambda \mathbf{B}''^{*}_{\mathbf{e}}, \sigma_e = \lambda \sigma^{*}_e, \qquad (37)$$

   where λ is scale factor given by

$$\lambda = \frac{Y}{\sigma_e^*}. \tag{38}$$

Including the first order effects of strain and pressure hardening the value of yield strength used in (38) can be expressed as

$$Y = Y^* + \left(\frac{\partial Y}{\partial \varepsilon_p}\right)\Delta\varepsilon_p + \left(\frac{\partial Y}{\partial p}\right)\Delta p. \tag{39}$$

We will only consider pressure change due to bulking since it may happen at constant volume. Unlike the changes in pressure proportional to the volume change, pressure changes due to bulking can cause a large difference in the amount of plastic strain calculated. The pressure increment is proportional to the porosity change during bulking; it is related to the plastic strain as

$$\Delta p \approx K\Delta\phi_u \frac{\partial\phi}{\partial\phi_u} = K\frac{\partial\phi}{\partial\phi_u}\dot{\phi}_{u2}\Delta\varepsilon_p, \tag{40}$$

where the plastic strain increment is expressed as

$$\Delta\varepsilon_p = (1-\lambda)\frac{\sigma_e^*}{3G}. \tag{41}$$

Thus, the yield strength at the end of the time step is a linear function of λ as

$$\begin{aligned} Y &= Y^* + A(1-\lambda) \\ A &= \frac{\sigma_e^*}{3G}\left(\frac{\partial Y}{\partial \varepsilon_p} + \frac{\partial Y}{\partial p}K\frac{\partial\phi}{\partial\phi_u}\dot{\phi}_{u2}\right). \end{aligned} \tag{42}$$

Substituting (42) into (38) gives the following expression for λ

$$\lambda = \frac{Y^* + A}{\sigma_e^* + A}. \tag{43}$$

6. Bulking porosity calculation

Using the bulking rate from step 4, and the increment in plastic strain found in the previous step, we next calculate the new value of unloaded bulking porosity.

7. **Pressure update**

   New unloaded porosity is used to find solid density and calculate new solid pressure with EOS

3. Simulation of static tests

Laboratory data [11] were used to calibrate the model. The model fit of experimental data for concrete is shown in Fig.3 and Fig.4 below.

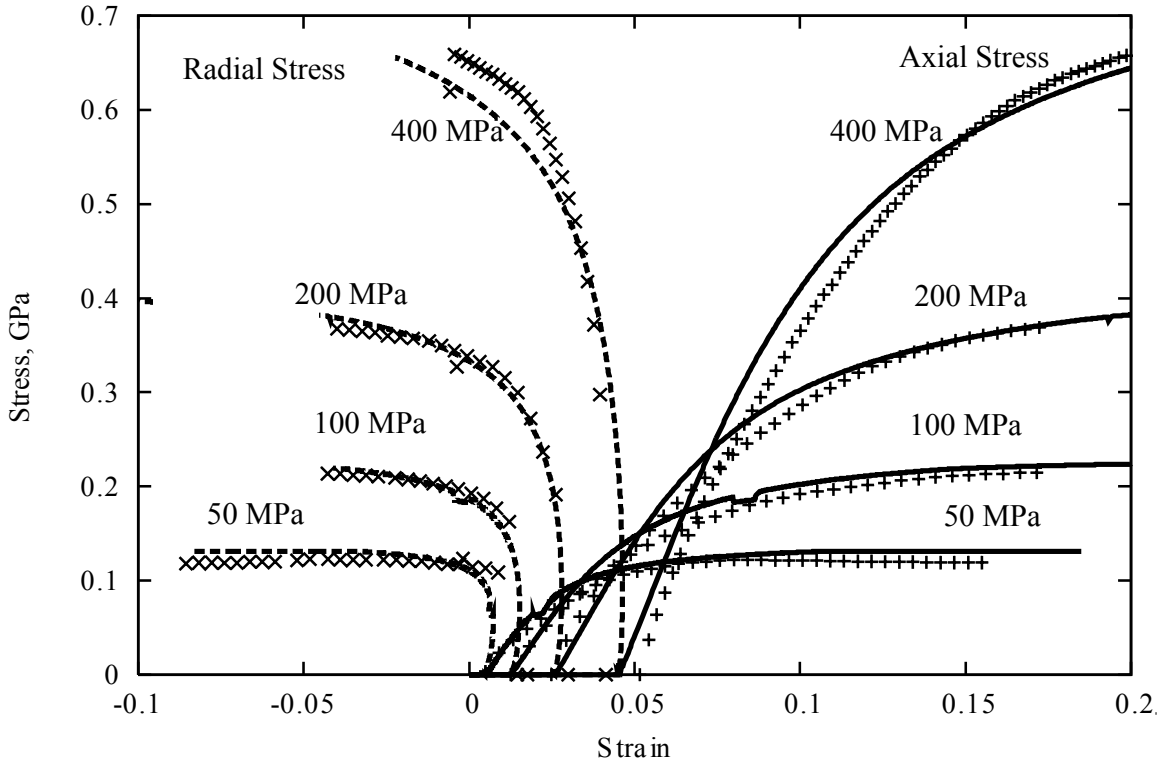

Fig.3 Experimental (markers) and calculated (lines) triaxial tests for concrete.

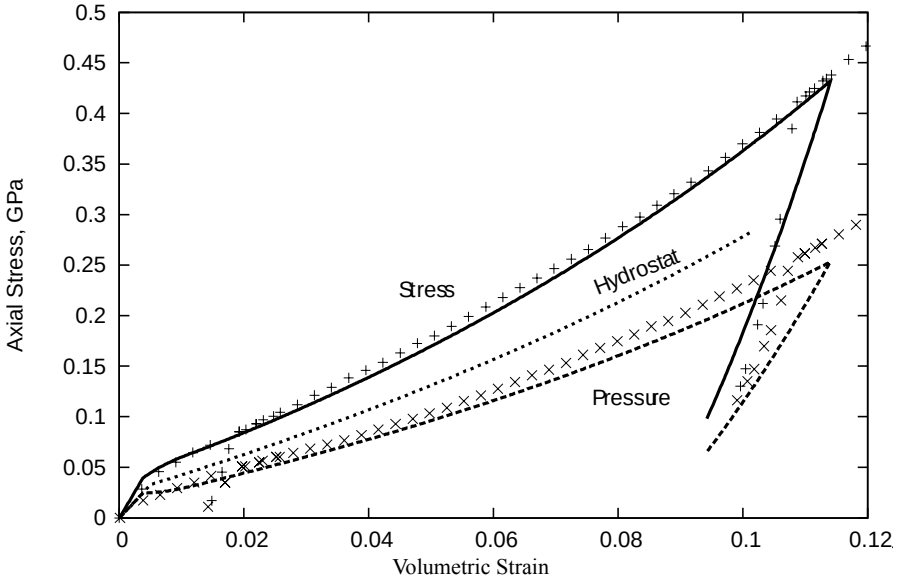

Fig.4 Uniaxial compression of concrete. Experimental points are shown with markers.

4. Spherical cavity expansion simulation

Spherical cavity expansion simulations are much simpler and much easier to perform than high fidelity penetration simulations using first principles codes. However, because cavity expansion simulations afford a reasonable approximation of the conditions at the nose of a penetrator, they are ideally suited for parameter sensitivity studies to examine trends in the model and to assess the effects of various parameters and physical processes on penetration.

Using the experimentral data presented in [11], we performed a series of cavity expansion simulations. A Lagrangian mesh containing 2000 quadrilateral elements with 2121 nodes was used. Radial velocity in the range from 100 m/s to 600 m/s was applied at the nodes along the cavity wall and a nonreflecting boundary condition was used at the outermost boundary of the computational domain. The purpose of these calculations is to find a forcing function that can be applied to the projectile to model its deceleration and

the final penetration depth. This method assumes that the loading path in a spherical cavity expansion problem is very similar to one at the nose of the projectile. However, our model includes strength softening, so that the stress reaches a maximum before it decreases approaching a constant value corresponding to the failed material as it is shown in Fig.5. In this case, it is not clear how to derive the forcing function from the cavity expansion. Figure 6 shows both maximum and final stresses as functions of the cavity velocity as well as analytical fits for the calculated points with quadratic functions. The same picture also shows the forcing function used in [11] and an improved forcing function, which gives better agreement with the experiment.

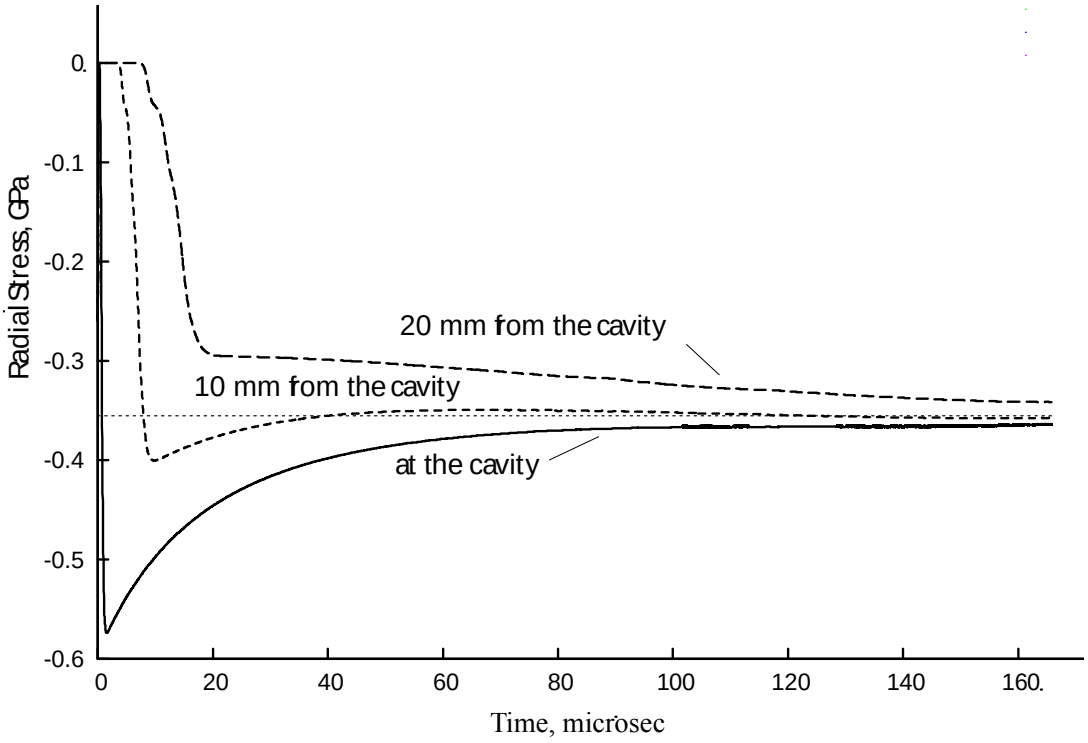

Fig.5 Radial Stress evolution for a cavity with an initial radius of 40 mm moving at a velocity of 200 m/s velocity.

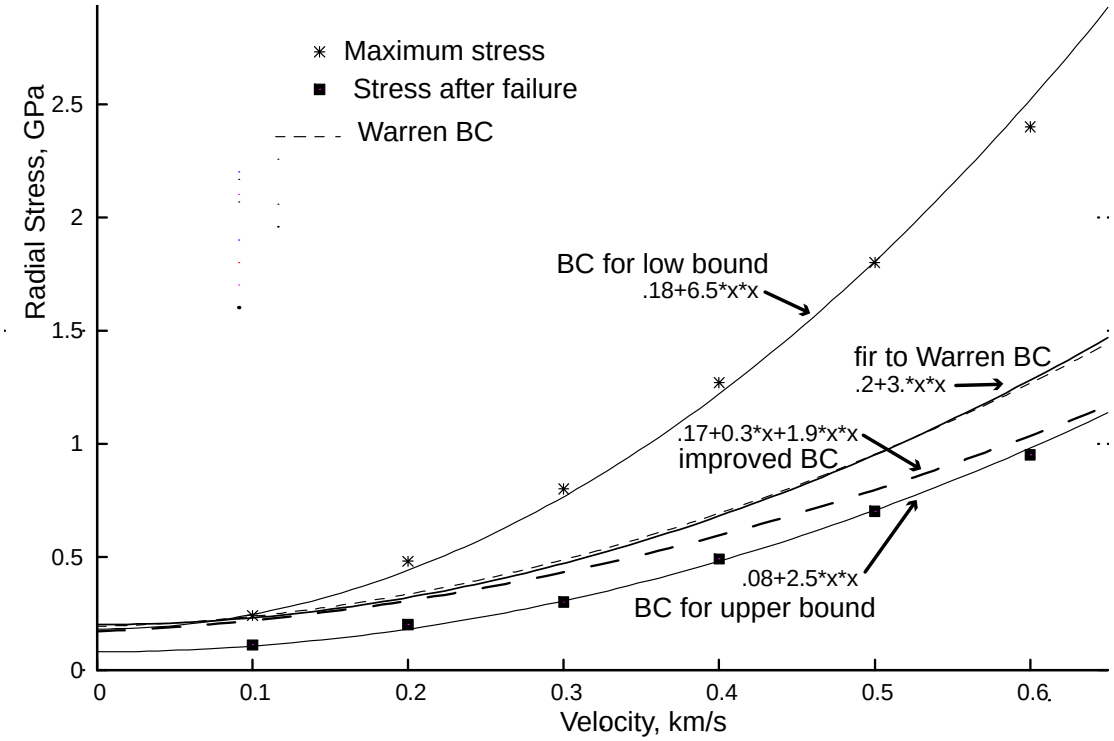

Fig.6 Calculated radial stress as a function of boundary velocity for the spherical cavity expansion problem. Points are calculations, and lines are analytic fits used in boundary conditions.

5. Simulation of penetration into low-strength (23 MPa) concrete

The model described in this paper was originally developed to model spherical explosions in porous geologic material, both in dry and saturated conditions. Numerical simulations of penetration into geologic media validate the model for another type of problem with a more complex loading path. It turns out that some parameters in the model that did not significantly affect spherical wave propagation or static test results under a wide range of triaxial loading histories, have a much greater effect on the results of penetration simulations. The most important parameter is the softening rate D in Eq. (18)

Figure 7 shows both the results of spherical cavity expansion model and the hydrocode calculations with the material model described in this paper. Dashed lines show analytical results obtained using three different forcing functions and the method described in [9]. The "upper bound" curve is based on the forcing function shown in Fig.6 with the lowest curve. The "low bound" curve is based on the forcing function shown in Fig.6 with the highest curve. And the dashed curve in the middle was obtained using the same forcing functions as described in the paper of Warren et. al. [11]. Experimental data points in the figure are identified with 'X' symbols. The "+" symbols identify results of Lagrangian spherical cavity expansion calculations with SANDIA's PRONTO hydrocode as described in [11]. The bold solid line represents our Lagrangian calculations with the same boundary conditions, and the thin solid line shows our calculations with the improved boundary conditions. The Squares show our hydrocode simulation results performed with GEODYN –eulerian AMR hydrocode.

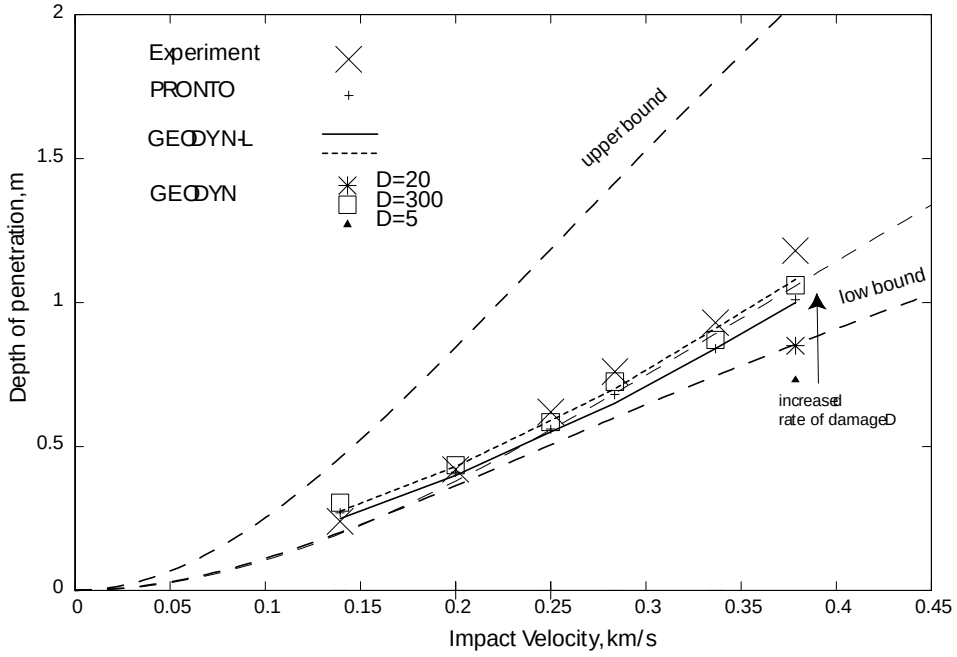

Fig.7 Experimental and calculated depth of penetration for various impact velocities.

6. Conclusion

We have demonstrated that the model developed can successfully predict penetration into porous geologic materials. Effects of strength softening, bulking and porous compaction are important to reproduce correct penetration depth in the calculations.

Spherical cavity expansion method is useful for the parameter sensitivity study but is not a suitable substitute to high fidelity numerical modeling of the penetration because of complexity in material behavior.

References

1. Rubin M.B., Elata D., Attia A.V. "Modeling added compressibility of porosity and the thermomechanical response of wet porous rock with application to Mt.Helen Tuff", *Int.J.Solids Structures* Vol.33 (6) pp.761-793 (1996)

2. Hoek, E., and Brown, E.T., "Empirical Strength Criterion for Rock Masses", *Journal of the Geotechnical Engineering Division*, American Society of Civil Engineers, Vol.106(GT9), pp.1013-1035 (1980b)

3. Hoek, E.,"Strength of Rock Masses", *International Society of Rock Mechanics News Journal*, Vol.2(2), pp.4-16 (1994)

4. Hoek,E.,Carranza-Torres, C.,Corkum B. "Hoek_Brown Failure Criterion-2002 edition", in *NARMS-TAC 2002: Mining and Tunnelling Innovation and Opportunity*, Vol. 1, pp. 267-273. R. Hammah et al., Eds. Toronto: University of Toronto Press (2002)

5. Mogi, K., “Pressure Dependence of Rock Strength and Transition from Brittle Fracture to Ductile Flow”, *Bull.Earthquake Research Institute*, (44)Part1, pp. 215-232 (1966)

6. Malvar L.J., Crawford J.E., Wesevich J.W., Simons D. “A Plasticity concrete material model for DYNA3D”, *Int.J.Impact Engng* vol.19(9-10),pp.847-873 (1997)

7. Vorobiev O.Yu, Lomov I.N.,Glenn L.A., Rubin M.B “Numerical Integration of an Elastic-Viscoplastic model with Stiff Hardening and Softening” in *Advances in Computational Engineering Sciences*, edt. S.N.Atluri and F.W. Brust,Tech Science Press, Palmdale (2000)

8. Rubin M.B., Vorobiev, O.,Yu., Glenn L.A., “Mechanical and Numerical modeling of a porous elastic-viscoplastic material with tensile failure”, *Int.Journ.of Solids and Structures*, Vol.37,pp.1841-1871,(2000)

9. Forrestal M.J., Tzou D.Y., Askari E. and Longcope D.B., “Penetration into ductile metal targets with rigid spherical-nose rods”, *Int.J.Impact Engng* (1995), Vol.16 (5-6),pp.699-710

10. Forrestal M.J., Frew D.J., Hickerson J.P., Rohwer T.A “Penetration of concrete targets with deceleration-time measurements”, *Int.J.Impact.Eng* (2003),vol.28,pp479-97

11. Warren T.L., Fossum A.F., Frew D.J. “ Penetration into low-strength (23Mpa) concrete:target characterization and simulations”, *Int.J.Impact.Engng.(2004),* Vol.30, (5), pp 477-503

This work was performed under the auspices of the U.S. Department of Energy by University of California, Lawrence Livermore National Laboratory under contract W-7405-Eng-48.